RESEARCH ARTICLE

Enabling efficient near-infrared emission in lead-free double perovskite *via* a codoping strategy†

Xiangyan Yun,[a,b] Hanlin Hu, [iD][c] Haizhe Zhong,[b] Jingheng Nie,*[d] Henan Li[e] and Yumeng Shi [iD] *[a,e]

Metal halides show great promise as a new generation of near-infrared (NIR) light-emitting materials. Compared with other light-emitting materials, double perovskites possess structures with different dimensionalities, which can support multiple emission centers, leading to varied photoluminescence. Among various doping centers, ytterbium(III) (Yb^{3+}) has attracted attention because of its unique two-energy-level structure ($^2F_{5/2}$ and $^2F_{7/2}$). However, the NIR emission of Yb^{3+} remains unsatisfactory because of poor resonance energy transfer between Yb^{3+} and sensitizers. Here, effective NIR-emitting lead-free perovskites are developed by co-doping antimony(III) (Sb^{3+}) and lanthanide(III) ions into $Cs_2NaInCl_6$. Under excitation at 318 nm, $Cs_2NaInCl_6:Sb^{3+}/Yb^{3+}$ showed a broadband NIR emission peak at 1001 nm, whereas $Cs_2NaInCl_6:Sb^{3+}/Nd^{3+}$ exhibited three NIR emission peaks at 896, 1077, and 1358 nm. The exciton dynamics of the materials were investigated. Experiments and density functional theory calculations revealed that the NIR emission of Yb^{3+} originated from a charge-transfer state (CTS) and energy transfer, whereas that of Nd^{3+} arose from resonance energy transfer. Profiting from the high-energy self-trapped exciton (STE) emission and CTS with Yb^{3+}, a high photoluminescence quantum yield of 48.95% was realized. The excellent NIR luminescence performance combined with high environmental stability demonstrates the potential of these metal halides for use in night-vision technologies.

1. Introduction

All-inorganic metal halide perovskites are promising materials for light-emitting technologies because of their excellent

[a]*Key Laboratory of Luminescence and Optical Information Ministry of Education Institute of Optoelectronic Technology, Beijing Jiaotong University, Beijing 100044, P. R. China. E-mail: ymshi@bjtu.edu.cn*
[b]*International Collaborative Laboratory of 2D Materials for Optoelectronics Science and Technology of Ministry of Education, Institute of Microscale Optoelectronics, Shenzhen University, Shenzhen 518060, P. R. China*
[c]*Hoffman Institute of Advanced Materials, Shenzhen Polytechnic, Shenzhen 518060, P. R. China*
[d]*Guangdong Rare Earth Photofunctional Materials Engineering Technology Research Center, School of Chemistry and Environment, Jiaying University, Meizhou, 514015, P. R. China. E-mail: niejh@jyu.edu.cn*
[e]*School of Electronics and Information Engineering, Shenzhen University, Shenzhen 518060, P. R. China*
†Electronic supplementary information (ESI) available: Experimental section, PLQYs testing and calculation, photographs of $Cs_2NaInCl_6:Sb^{3+}/Ln^{3+}$ (Ln^{3+} = Yb^{3+}, Nd^{3+}) single crystals, PXRD patterns, SEM image and EDX elemental mappings, PLE spectra, NIR PL decay, PLQYs, Ultraviolet–visible absorption spectra of $Cs_2NaInCl_6:Sb^{3+}/Ln^{3+}$ (Ln^{3+} = Yb^{3+}, Nd^{3+}) single crystals, PL and PLE mapping of $Cs_2NaInCl_6:Sb^{3+}/Ln^{3+}$ (Ln^{3+} = Yb^{3+}, Nd^{3+}) single crystals, PLE spectra of $Cs_2NaInCl_6:Sb^{3+}/Ln^{3+}$ (Ln^{3+} = Er^{3+}, Ho^{3+}, Nd^{3+}, Yb^{3+}), energy-level diagrams, PDOS, ICP elemental analysis of $Cs_2NaInCl_6:Sb^{3+}/Ln^{3+}$ (Ln^{3+} = Yb^{3+}, Nd^{3+}) single crystals, NIR PLQYs of metal halides (PDF). See DOI: https://doi.org/10.1039/d4qi01518e

photophysical properties such as high photoluminescence quantum yield (PLQY), tunable light emission wavelength, and cost-effective synthesis.[1–4] Presently, the development and preparation techniques for visible light-emitting perovskites are relatively mature, adequately meeting demands in areas such as illumination and displays.[5–7] However, the evolving needs of medical imaging, optical communications, optical storage, military reconnaissance, security monitoring, and sensing generate demand for lead-free near-infrared (NIR)-emitting metal halide perovskites.[8–11] This demand arises from the advantageous properties of NIR light sources, such as strong penetration, minimal biological damage, and high resolution.[12–14] NIR light-emitting diodes (LEDs) that can be used for full-spectrum (400–1100 nm) illumination, infrared security anti-counterfeiting, and infrared imaging have emerged as a burgeoning area of research.[15] The most commonly used method for achieving NIR luminescence from perovskites involves doping with lanthanide or transition metal ions.[16–18] However, the traditional ABX_3 perovskite structure cannot meet the requirements of trivalent-ion dopants.[19] Consequently, a strategy of heterovalent double-cation co-substitution (*e.g.*, $B^+ + B'^{3+} \rightarrow Pb^{2+} + Pb^{2+}$) has been adopted to fabricate stable inorganic double-perovskite systems ($A_2BB'X_6$).[20–22] The challenges of low PLQY and restricted emission range have emerged as technological bottlenecks in the devel-

6146 | *Inorg. Chem. Front.*, 2024, **11**, 6146–6155

This journal is © the Partner Organisations 2024

opment of NIR-emitting perovskites.[23] Thus, the pursuit of an effective method to achieve high-efficiency, long-wavelength NIR emission holds paramount importance for expanding the applications of NIR technology.

Currently, lanthanide ions (Ln^{3+}; *e.g.*, Er^{3+}, Ho^{3+}, Tm^{3+}, Sm^{3+}, Dy^{3+}, Yb^{3+}, Nd^{3+}) and transition metal ions (*e.g.*, Mn^{4+}, Cr^{3+}, Cr^{4+}) are popular activators for NIR luminescence.[24–26] However, achieving high PLQYs in halide matrices with these activator ions through single ion-doping strategies is rarely possible. Energy transfer (ET) is an effective approach to improve NIR PLQY and extend the emission wavelength range of metal halides.[27,28] For example, NIR luminescence was achieved by co-doping Te^{4+} and Nd^{3+} into a Cs$_2$ZrCl$_6$ host; ET from yellow-emitting Te^{4+} to NIR-emitting Nd^{3+} was clearly observed.[29] The simple energy-level structure (^{2}F$_{5/2}$ and ^{2}F$_{7/2}$) of Yb^{3+}, which helps to suppress non-radiative energy losses, has led to it becoming a popular activator ion in the field of NIR luminescence.[30–32] However, the NIR PLQYs and ET efficiency of Yb^{3+}-doped materials remain low because of the reliance of the traditional resonant ET mechanism on the degree of overlap between the emission band of the photoreceptor and absorption band of the activator. For example, while Bi^{3+}/Yb^{3+}-co-doped Cs$_2$Na$_{0.6}$Ag$_{0.4}$InCl$_6$ double perovskites showed enhanced NIR emission because of ET from self-trapped excitons (STEs) to Yb^{3+}, the ET efficiency was not ideal.[33,34] Therefore, suitable transfer strategies need to be identified to facilitate ET and obtain high-efficiency NIR emission.

Herein, high-efficiency NIR emission is achieved by co-doping Sb^{3+} and Ln^{3+} in Cs$_2$NaInCl$_6$. The Jahn–Teller deformation of the [SbCl$_6$]$^{3-}$ octahedron in the STE process leads to efficient formation of ET channels, enabling efficient NIR luminescence from Ln^{3+} in Cs$_2$NaInCl$_6$:Sb^{3+}. With the help of a charge-transfer state (CTS) of Yb^{3+}, efficient NIR emission at 1001 nm with a high PLQY of 48.95% is obtained from Cs$_2$NaInCl$_6$:Sb^{3+}/Yb^{3+} under 318 nm excitation. In addition, three NIR emission peaks at 896, 1077, and 1358 nm with a high PLQY of 11.29% are exhibited by Cs$_2$NaInCl$_6$:Sb^{3+}/Nd^{3+} under 318 nm excitation. Experimental and density functional theory (DFT) calculation results reveal that the NIR emission of Yb^{3+} could be derived from a CTS and ET, whereas that of Nd^{3+} could originate from resonance ET.

2. Results and discussion

Cs$_2$NaInCl$_6$ crystallizes into a cubic structure (space group: $Fd\bar{3}m$) consisting of alternating [InCl$_6$]$^{3-}$ and [NaCl$_6$]$^{5-}$ octahedra with large Cs$^+$ occupying the center of the cuboctahedral cavities (Fig. 1a).[35] High-quality Cs$_2$NaInCl$_6$:Sb^{3+}/Ln^{3+} (Ln^{3+} = Nd^{3+} or Yb^{3+}) single crystals were prepared *via* a facile hydrothermal synthesis method (Fig. S1†). Sb^{3+} and Ln^{3+} tend to occupy the In^{3+} sites because of their similar ionic radii and valence.[36] Powder X-ray diffraction (PXRD) measurements showed that all diffraction peaks matched well with the standard pattern of Cs$_2$NaInCl$_6$ (ICSD#132718). With increasing Nd^{3+} or Yb^{3+} content, the diffraction peaks shifted to lower

angles because the ionic radii of Nd^{3+} (98 pm) and Yb^{3+} (87 pm) are larger than that of In^{3+} (80 pm), as shown in Fig. S2 and S3.†[37] Scanning electron microscopy (SEM) images showed that the samples were polyhedral with mean sizes of about 5 μm. Energy-dispersive X-ray spectroscopy (EDS) elemental mapping revealed that the dopants were homogeneously distributed in the samples (Fig. 1c and S4–S6†). These results suggest the successful incorporation of Sb^{3+} and Ln^{3+} in the double perovskite crystal lattice. The dopant concentrations were estimated by inductively coupled plasma mass spectrometry (ICP-MS); the results are listed in Tables S1 and S2.† The ICP-MS results are similar to the EDS element content results, and the accuracy of the measurement is verified again (Table S3†). The actual content of Ln^{3+} in the samples is shown in Fig. 1d. There was a considerable difference between the actual doping concentration of the Cs$_2$NaInCl$_6$:Sb^{3+}/xLn^{3+} samples and the feed ratio of Yb^{3+} and Nd^{3+}. Similar trends have been reported for doped halides such as Cs$_2$KInCl$_6$:Sb^{3+}/Ho^{3+}, Cs$_2$AgInCl$_6$:Cr^{3+}/Er^{3+}, and Cs$_2$ZrCl$_6$:Sb^{3+}/Nd^{3+}.[38–40] The doping ratio stated in this study refers to the feed ratio of Ln^{3+} rather than the actual doping concentration.

To explore the photophysical process of Cs$_2$NaInCl$_6$:Sb^{3+}/Ln^{3+} in detail, photoluminescence spectra in the visible and NIR regions were recorded. The PLQY of the Cs$_2$NaInCl$_6$ matrix at RT was less than 1%. The Sb^{3+}-doped sample showed a high-energy blue emission peak at 446 nm with a full width at half maximum (FWHM) of 128 nm (Fig. S7†), which was attributed to the STE emission in the [SbCl$_6$]$^{3-}$ octahedra caused by strong Jahn–Teller lattice distortion.[41] Under 318 nm excitation, in addition to the blue emission, an intense NIR emission at 1001 nm was observed in Sb^{3+}/Yb^{3+}-co-doped Cs$_2$NaInCl$_6$, which was assigned to the ^{2}F$_{5/2}$ → ^{2}F$_{7/2}$ transitions of Yb^{3+} (Fig. 2a and b).[31] As shown in Fig. 2c, the STE emission intensity decreased and the NIR emission intensity greatly increased as the Yb^{3+} doping content increased to 60%. Higher Yb^{3+} doping concentration than 60% led to a decrease in NIR efficiency because of concentration quenching. The Sb^{3+}/Nd^{3+}-co-doped Cs$_2$NaInCl$_6$ samples displayed a blue emission peak at 446 nm and three sharp NIR emission bands at 896, 1077, and 1358 nm, which were assigned to the ^{4}F$_{3/2}$ → ^{4}I$_{9/2}$, ^{4}F$_{3/2}$ → ^{4}I$_{11/2}$, and ^{4}F$_{3/2}$ → ^{4}I$_{13/2}$ transitions of Nd^{3+}, respectively (Fig. 2d and e).[42] The NIR emission signals exhibited millisecond-scale lifetimes of 3.29 ms for that originating from Yb^{3+} and 4.08 ms for that derived from Nd^{3+} (Fig. S8 and S9†), which were characteristic of Laporte forbidden f–f transitions.[32,40] The NIR emission intensity greatly increased and STE emission intensity decreased with increasing Nd^{3+} content, as depicted in Fig. 2e. Both Sb^{3+}/Yb^{3+} and Sb^{3+}/Nd^{3+} co-doped samples showed excellent NIR luminescence properties. The highest NIR emission intensity of Sb^{3+}/Yb^{3+}-co-doped samples with a PLQY of 48.95% was obtained when the Yb^{3+} feed ratio was 60% (Fig. S10†). It has shown good performance in the recently reported NIR PLQY of metal halides (Table S4†). The highest NIR PLQY of Sb^{3+}/Nd^{3+}-co-doped Cs$_2$NaInCl$_6$ of 11.29% was obtained when the Nd^{3+} feed

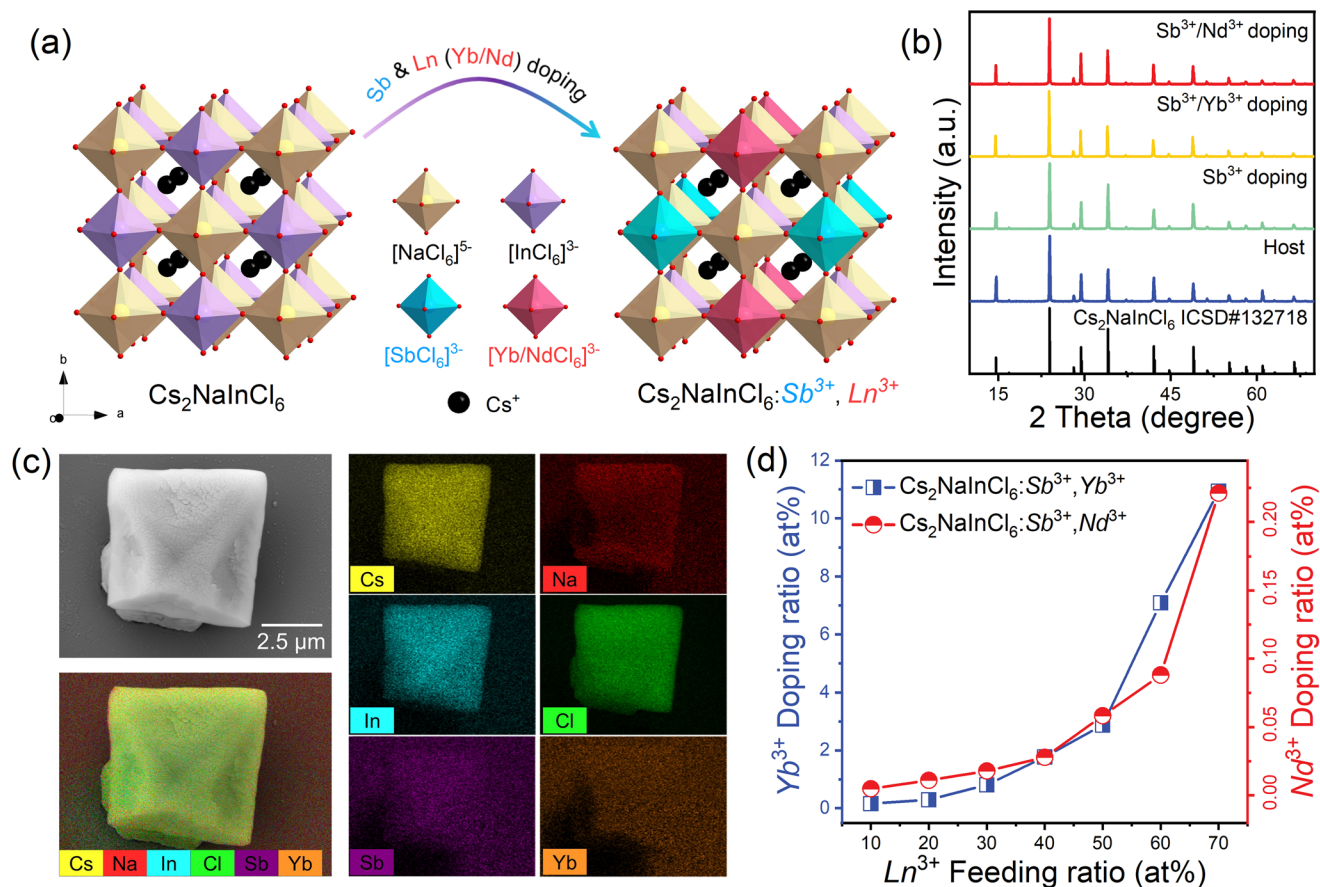This journal is © the Partner Organisations 2024

Inorg. Chem. Front., 2024, **11**, 6146–6155 | **6147**

Fig. 1 (a) Schematic illustrations of $Cs_2NaInCl_6$ crystal structures with Sb^{3+} and Ln^{3+} (Ln = Yb, Nd) doping. (b) The PXRD patterns of host, Sb^{3+}-doped, Sb^{3+}/Yb^{3+} co-doped, and Sb^{3+}/Nd^{3+} co-doped $Cs_2NaInCl_6$. (c) SEM image and EDX elemental mappings (Cs, Na, In, Cl, Sb, Yb, and merge) of $Cs_2NaInCl_6$:Sb^{3+}/Yb^{3+}. (d) ICP-MS results of Ln^{3+} amount in $Cs_2NaInCl_6$:Sb^{3+}/Yb^{3+} and $Cs_2NaInCl_6$:Sb^{3+}/Nd^{3+}.

ratio was 70% (Fig. S11†). The sensitization induced by Sb^{3+} caused the NIR emission intensity of Sb^{3+}/Yb^{3+} and Sb^{3+}/Nd^{3+} co-doped samples to increase considerably compared to that of Yb^{3+} or Nd^{3+} singly doped samples (Fig. S12 and S13†).

To reveal the luminescence mechanism of the samples, absorption and photoluminescence excitation (PLE) spectra of the co-doped samples were collected. As shown in Fig. 3a, Yb^{3+} singly doped $Cs_2NaInCl_6$ exhibited an additional absorption peak at about 270 nm compared to the absorption spectra of undoped and Nd^{3+} singly doped $Cs_2NaInCl_6$, matching closely with the PLE spectra (Fig. 3b). The excitation band at 266 nm corresponded to the Yb^{3+} absorption of the $Cl^- \rightarrow Yb^{3+}$ CTS.[29,43,44] Sb^{3+}/Yb^{3+} and Sb^{3+}/Nd^{3+} co-doped $Cs_2NaInCl_6$ samples exhibited an intense absorption peak at 320 nm, which was attributed to Sb^{3+}. As the feed ratio of Ln^{3+} rose, the actual doping concentration of Sb^{3+} increased (Tables S1 and S2†), and thus the corresponding absorption peak of Sb^{3+} increased in intensity at high Ln^{3+} doping concentration, as shown in Fig. S14 and S15.† The PLE spectrum monitored at 446 nm displayed characteristic excitation bands at 318 and 333 nm, which were assigned to the $^1S_0-^3P_1$ transition of Sb^{3+} (PLE spectra are shown in Fig. S16 and S17†). The PLE spectrum of Sb^{3+}/Nd^{3+} co-doped $Cs_2NaInCl_6$ monitored at 1077 nm

contained two weak narrow excitation peaks at 534 and 588 nm, consistent with that of Nd^{3+} singly doped $Cs_2NaInCl_6$, which were attributed to the direct excitation of Nd^{3+}.[42] The PLE spectra of visible (446 nm) and NIR (1077 nm) emissions were similar (Fig. 3c), indicating that these emissions have the same excited-state origin. Notably, the emission of Ln^{3+} originating from the f–f transition is usually sensitive to the excitation wavelength, while the emission spectra were almost constant with the variation of the excitation wavelength (Fig. 3e), suggesting that the NIR luminescence of Nd^{3+} mainly depends on the sensitization of Sb^{3+}. In addition, the excitation intensities at 534 and 588 nm were much lower than that at 318 nm, indicating that Nd^{3+} excitation through ET was more efficient than direct excitation. Because of the wide excitation range and high absorption strength of STE emission in the Sb^{3+}/Nd^{3+} co-doped $Cs_2NaInCl_6$ system, the weak absorption of the f–f transition can be overcome by the efficient ET, thus realizing efficient NIR luminescence. Notably, however, the NIR efficiency is still relatively low, which may be related to the small overlap between the emission region of Sb^{3+} and absorption region of Nd^{3+} limiting the ET efficiency.

Interestingly, the PLE spectra of the Sb^{3+}/Yb^{3+}-co-doped sample for the emissions at 446 and 1001 nm showed different
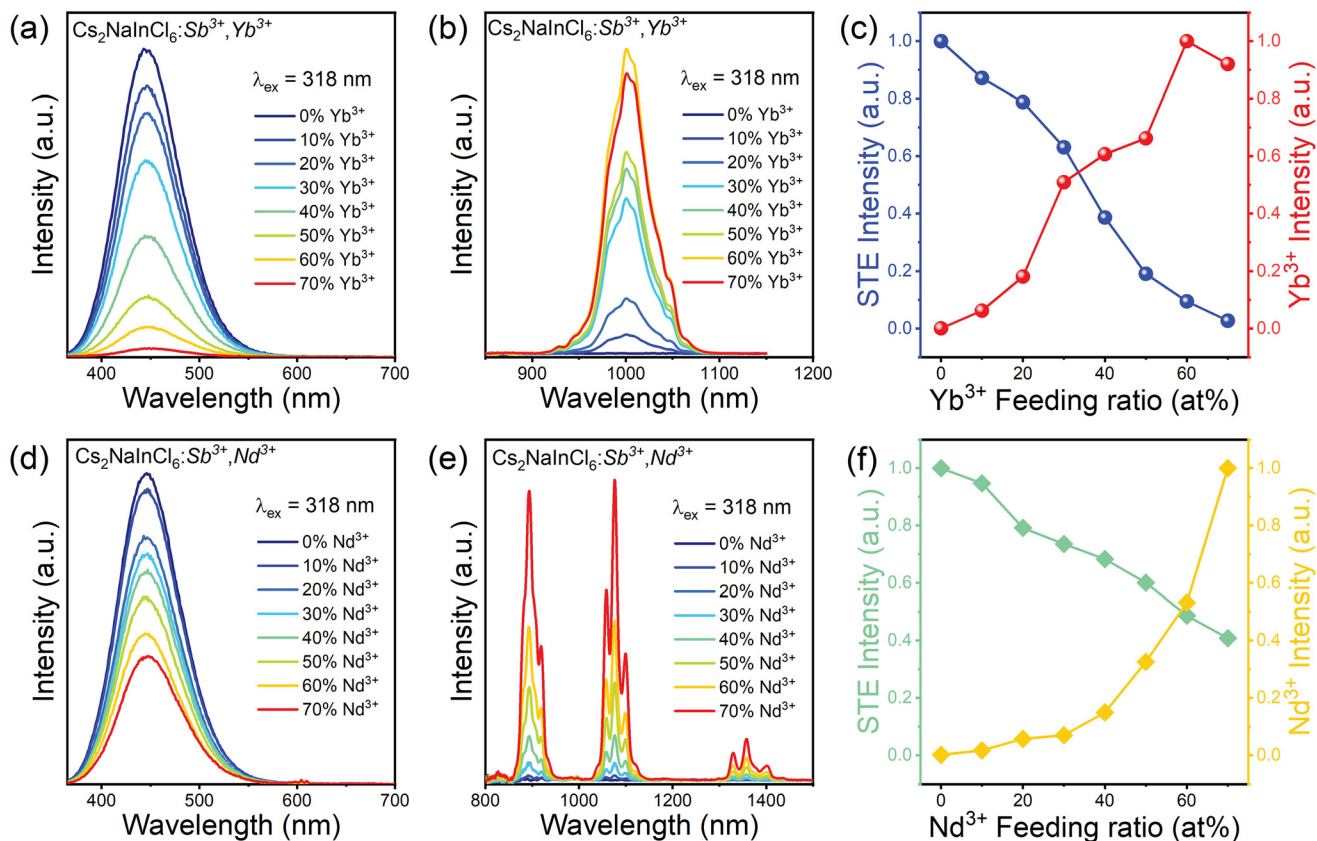
6148 | *Inorg. Chem. Front.*, 2024, **11**, 6146–6155

This journal is © the Partner Organisations 2024

Fig. 2 (a) Visible and (b) NIR emission spectra of $Cs_2NaInCl_6$:Sb^{3+}/Yb^{3+}. (c) Integrated PL intensities of visible and NIR emission of $Cs_2NaInCl_6$:Sb^{3+}/Yb^{3+} under 318 nm excitation. (d) Visible and (e) NIR emission spectra of $Cs_2NaInCl_6$:Sb^{3+}/Nd^{3+}. (f) Integrated PL intensities of visible and NIR emission of $Cs_2NaInCl_6$:Sb^{3+}/Nd^{3+} under 318 nm excitation.

patterns. Sb^{3+}/Yb^{3+}-co-doped $Cs_2NaInCl_6$ showed a broadband excitation above 300 nm, which was consistent with the excitation of Sb^{3+}-doped $Cs_2NaInCl_6$. This result implies that STE and NIR emissions could originate from the same excited state, and an ET process occurs from Sb^{3+} to Yb^{3+}.[45] The PLE spectrum of Sb^{3+}/Yb^{3+}-co-doped $Cs_2NaInCl_6$ displayed an additional excitation peak at 273 nm, which may originate from the $Cl^- \rightarrow Yb^{3+}$ CTS. As shown in Fig. 3d, the photoluminescence and PLE pseudo-color maps further confirmed that the NIR emission can be realized by ET and CTS. The characteristic excitation peaks of Yb^{3+} are different to those of other Ln^{3+}, as shown in Fig. S18.† Yb^{3+} has only two energy levels, $^2F_{5/2}$ and $^2F_{7/2}$, whereas other Ln^{3+} (*e.g.*, Er^{3+}, Ho^{3+}, Nd^{3+}) typically possess abundant 4f electronic states (Fig. S19†). Because Yb^{3+} has no energy levels that match the $^3P_1$ state of Sb^{3+}, Förster resonance ET from Sb^{3+} to Yb^{3+} was difficult. The spectral characteristics of the Sb^{3+}/Yb^{3+}-co-doped $Cs_2NaInCl_6$ system exhibit certain similarities to those reported for Cs_2ZrCl_6:Te^{4+}/Yb^{3+} halides.[29]

To further determine the ET process in the co-doped samples, time-resolved photoluminescence measurements of STE emissions were recorded. As shown in Fig. 4a and b, the excitation lifetime monitored at 446 nm shortened as the Ln^{3+} content increased (Tables S5 and S6†), implying that the

improved ET from the STEs to Ln^{3+} promoted decay of the STE emission.[46] The ET efficiency (η_T) from STE to Ln^{3+} can be calculated using the following equation:

$$\eta_T = 1 - \frac{\tau_x}{\tau_0} \tag{1}$$

where τ_0 and τ_x are the lifetimes of STE emission in the absence and presence of Ln^{3+}, respectively. η_T increases with the concentration of Yb^{3+} or Nd^{3+}, reaching 43.96% at 70% Yb^{3+} doping and 6.35% at 70% Nd^{3+} doping (Fig. 4c and d). It is noticed that, η_T of Sb^{3+}/Yb^{3+} is considerably higher than that of Sb^{3+}/Nd^{3+}, which is likely due to the possible CTS of Yb^{3+} as reported previously. For the Sb^{3+}/Yb^{3+}-co-doped system, it is difficult to achieve resonance ET because of the mismatched excitation energy-level between Yb^{3+} and Sb^{3+}. However, efficient NIR luminescence can be achieved *via* CTS of Yb^{3+}, which is similar to the ET process between Ce^{3+} (~400 nm) and Yb^{3+} (~980 nm) in a traditional phosphor system.[47–49] Schematic diagrams of the possible light emission mechanism are presented in Fig. 4e and f. Upon ultraviolet (UV) excitation at 300–380 nm, electrons are excited from the ground state to the excited states of Sb^{3+} and then trapped in $[SbCl_6]^{3-}$ octahedra through nonradiative relaxation, resulting in high-energy blue STE emission.[50] Simultaneously, benefiting from the

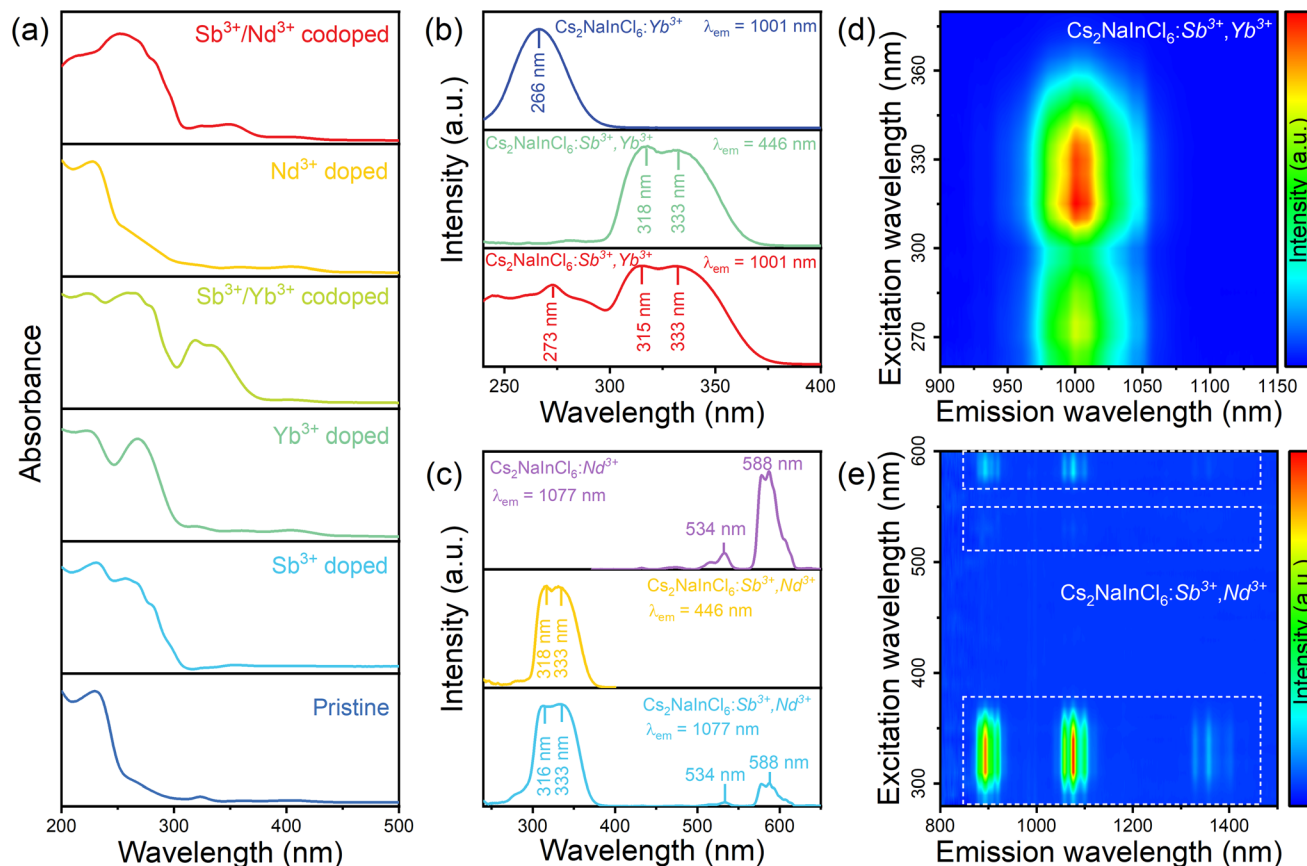This journal is © the Partner Organisations 2024

Inorg. Chem. Front., 2024, **11**, 6146–6155 | **6149**

Fig. 3 (a) Optical absorbance spectra of undoped, Sb^{3+}-doped, Yb^{3+}-doped, Nd^{3+}-doped, Sb^{3+}/Yb^{3+} co-doped, and Sb^{3+}/Nd^{3+} co-doped $Cs_2NaInCl_6$. Normalized PLE spectra of (b) Yb^{3+}-doped and Sb^{3+}/Yb^{3+} co-doped $Cs_2NaInCl_6$, (c) Nd^{3+}-doped and Sb^{3+}/Nd^{3+} co-doped $Cs_2NaInCl_6$. Contour plot of the excitation-dependent NIR emission of (d) $Cs_2NaInCl_6$:Sb^{3+}/Yb^{3+}, and (e) $Cs_2NaInCl_6$:Sb^{3+}/Nd^{3+}.

efficient ET channel from Sb^{3+} to Ln^{3+}, part of the energy can be transferred to Yb^{3+} or Nd^{3+} to emit NIR luminescence at 1001 nm ($^2F_{5/2} \rightarrow {}^2F_{7/2}$ transition of Yb^{3+}) or at 896, 1077, and 1358 nm (the transitions of Nd^{3+} from $^4F_{3/2}$ to $^4I_{9/2}$, $^4I_{11/2}$, and $^4I_{13/2}$ energy levels, respectively). Additionally, NIR emission at 1001 nm can also be achieved by $Cl^- \rightarrow Yb^{3+}$ CTS under excitation around 270 nm. On the basis of this CTS and ET, efficient NIR luminescence can be obtained in Sb^{3+}/Yb^{3+}-co-doped $Cs_2NaInCl_6$.

To further unveil the photophysics of the Sb^{3+}–Ln^{3+} pair, DFT calculations were performed to reveal the electronic structure of $Cs_2NaInCl_6$:Sb^{3+}/Ln^{3+}. In the pure $Cs_2NaInCl_6$ system, the conduction-band minimum (CBM) is mainly composed of Cl p states and In s states and the valence-band maximum (VBM) mainly consists of Cl p orbitals, as shown in Fig. S20.† For the Sb^{3+}/Yb^{3+}- and Sb^{3+}/Nd^{3+}-co-doped systems, a new band consisting of the Cl p states and Sb lone-pair s states appears above the host valence band, while the $SbCl_6$ CBM appears in a gap deep in the host conduction band, as illustrated in Fig. 5. The highest occupied molecular orbitals are composed of Sb s and Cl p states and the lowest unoccupied molecular orbitals are composed of Sb p and Cl p states. Meanwhile, the 4f bands of Yb^{3+} or Nd^{3+} are located in the gap

between the CBM and VBM of $SbCl_6$, which provides the possibility to realize ET.[51–53] These calculation results demonstrate that the introduced Sb^{3+} can modulate the host electronic structure and the introduced Ln^{3+} are located in the gap between the CBM and VBM of $SbCl_6$, confirming the possibility of ET.

To illustrate a potential application of $Cs_2NaInCl_6$:Sb^{3+}/Ln^{3+}, NIR LEDs were fabricated. The prepared $Cs_2NaInCl_6$:Sb^{3+}/Yb^{3+} was coated on a commercially available 365 nm UV-LED chip. The as-fabricated LEDs exhibited strong luminescence, as shown in Fig. 6a. The NIR emission intensity increased with the drive current, showing excellent NIR emission performance (Fig. 6b). Fig. 6c shows NIR applications of $Cs_2NaInCl_6$:Sb^{3+}/Yb^{3+} using different cameras (visible and NIR) and light sources (natural and NIR). To demonstrate NIR anti-counterfeiting, a picture with the acronyms "SZU", "DLB", "NIR", and "LED" in different colors exhibited distinct patterns when illuminated by natural and NIR light. The principle behind this behavior is that the black "SZU" letters contained carbon black, resulting in strong absorption of NIR light. For infrared detection applications, the area of a picture covered by the long-wavelength filter was not detected by the visible camera under natural light. No image was captured by the NIR
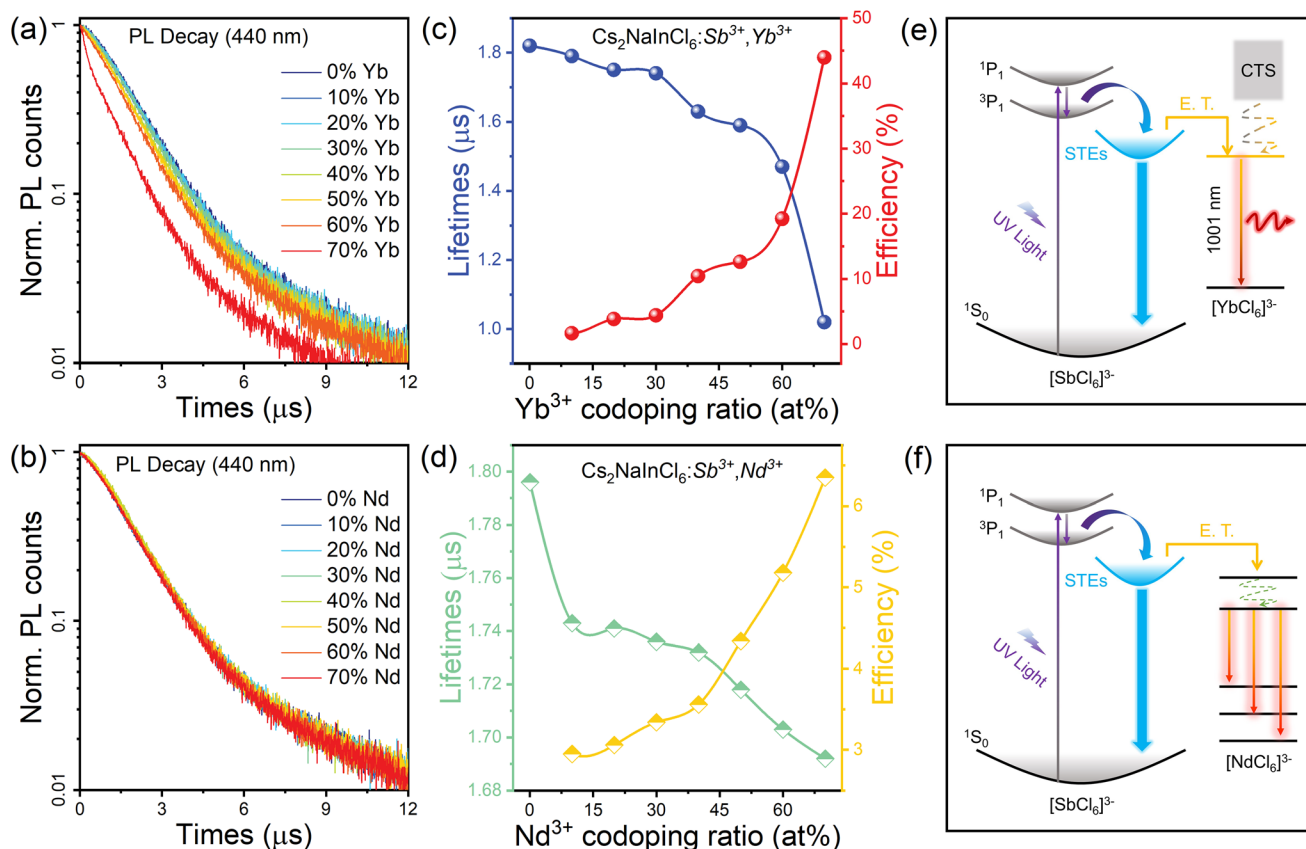
Fig. 4 PL decay curves (λ_{ex} = 318 nm, λ_{em} = 446 nm) of (a) Cs$_2$NaInCl$_6$:Sb^{3+}/Yb^{3+}, (b) Cs$_2$NaInCl$_6$:Sb^{3+}/Nd^{3+}. Lifetime of 446 nm and ET efficiency as a function of (c) Yb^{3+} concentration, and (d) Nd^{3+} concentration. Schematic representation of the photophysical process in (e) Cs$_2$NaInCl$_6$:Sb^{3+}/Yb^{3+}, (f) Cs$_2$NaInCl$_6$:Sb^{3+}/Nd^{3+}.
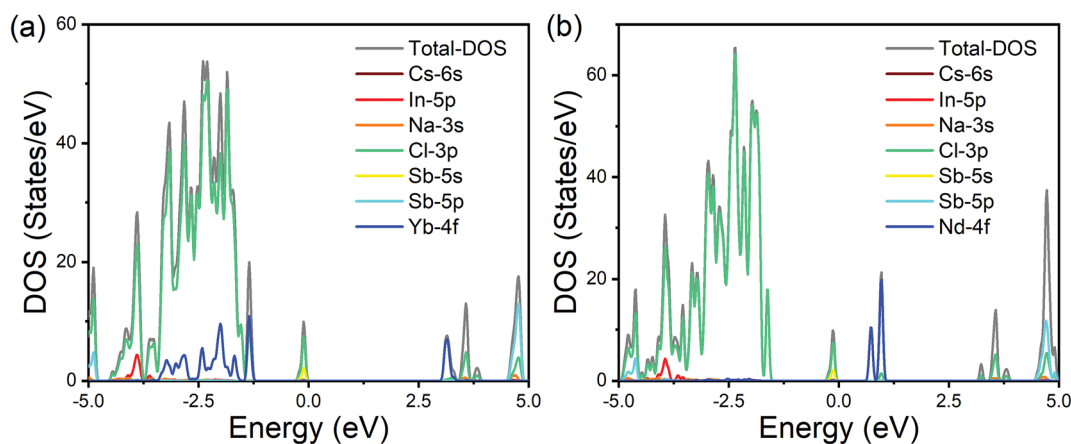
Fig. 5 DFT simulations. DOS of (a) Cs$_2$NaInCl$_6$:Sb^{3+}/Yb^{3+} sample and (b) Cs$_2$NaInCl$_6$:Sb^{3+}/Nd^{3+} sample.

camera when the NIR LEDs were switched off. In contrast, when the NIR LEDs were switched on, a clear and complete image was detected by the NIR camera. Similar detection applications can also be found in biology, where yellow-green leaf veins can be clearly captured using the NIR LEDs. To demonstrate night-vision applications, black-and-white photo-

graphs of fruit were captured upon illumination with the NIR LEDs. The image clarity was relatively high, with the images clearly displaying the contours of the photographed objects. These results reveal the great potential of the prepared Cs$_2$NaInCl$_6$:Sb^{3+}/Yb^{3+} samples for use in NIR anti-counterfeiting, infrared detection, and night-vision technologies. The

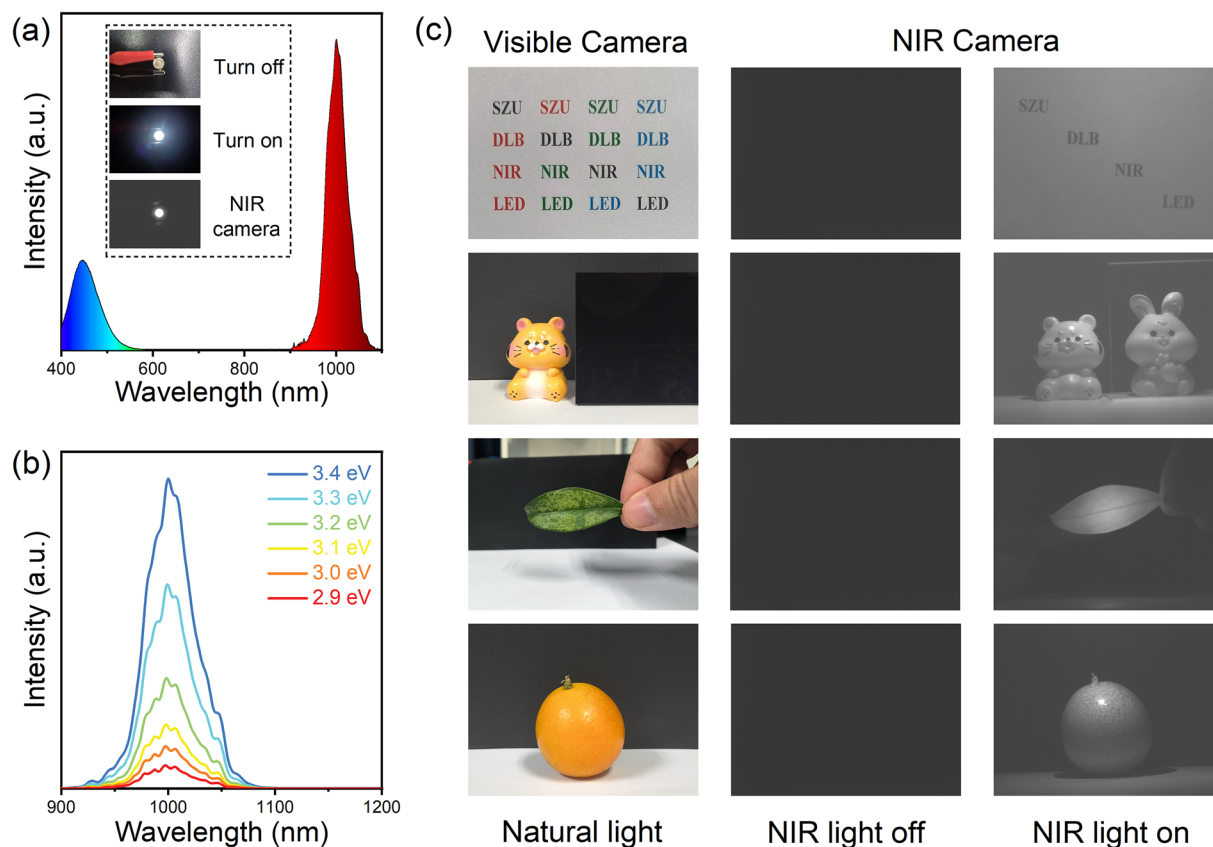This journal is © the Partner Organisations 2024

Inorg. Chem. Front., 2024, **11**, 6146–6155 | **6151**

Fig. 6 (a) Emission spectrum of as-fabricated LED based on $Cs_2NaInCl_6$:Sb^{3+}/Yb^{3+}. Inserts show the photographs of as-fabricated LED. (b) NIR emission spectrum for different operational voltages of as-fabricated LED. (c) Photographs captured by visible camera or NIR camera under daylight, in dark, and upon illumination with the LED combined with $Cs_2NaInCl_6$:Sb^{3+}/Yb^{3+}.

environmental stability of the $Cs_2NaInCl_6$:Sb^{3+}/Yb^{3+} and $Cs_2NaInCl_6$:Sb^{3+}/Nd^{3+} samples was evaluated. As shown in Fig. S21,† the PXRD peaks of the $Cs_2NaInCl_6$:Sb^{3+}/Yb^{3+} and $Cs_2NaInCl_6$:Sb^{3+}/Nd^{3+} samples remained unchanged after continuous illumination under 365 nm UV light. As shown in Fig. S22,† the PL performance of $Cs_2NaInCl_6$:Sb^{3+}/Yb^{3+} and $Cs_2NaInCl_6$:Sb^{3+}/Nd^{3+} samples were almost unchanged even upon heating at 420 K for 6.5 h. These experimental results indicate that $Cs_2NaInCl_6$:Sb^{3+}/Ln^{3+} perovskites are promising for NIR LED applications in advanced night-vision detection and anti-counterfeiting.

nated from resonance ET. Profiting from the high-energy STE emission and CTS of Yb^{3+}, the high NIR PLQY was realized by efficient ET from STEs to Yb^{3+}. The excellent NIR luminescence performance and high environmental stability of $Cs_2NaInCl_6$:Sb^{3+}/Yb^{3+} endow it with good application prospects in NIR anti-counterfeiting and night-vision devices.

Data availability

The data supporting this article have been included as part of the ESI.†

3. Conclusions

In summary, $Cs_2NaInCl_6$:Sb^{3+}/Yb^{3+} and $Cs_2NaInCl_6$:Sb^{3+}/Nd^{3+} single crystals that displayed efficient NIR emission were synthesized. Under excitation at 318 nm, $Cs_2NaInCl_6$:Sb^{3+}/Yb^{3+} showed a broadband NIR emission peak at 1001 nm with a high PLQY of 48.95%, whereas $Cs_2NaInCl_6$:Sb^{3+}/Nd^{3+} exhibited three NIR emission peaks at 896, 1077, and 1358 nm with a PLQY of 11.29%. The results of experiments and DFT calculations revealed that the NIR emission of Yb^{3+} was derived from a CTS and ET, whereas the NIR emission of Nd^{3+} origi-

Conflicts of interest

There are no conflicts to declare.

Acknowledgements

6152 | *Inorg. Chem. Front.*, 2024, **11**, 6146–6155

This journal is © the Partner Organisations 2024

References

1 Z. Yuan, C. K. Zhou, Y. Tian, Y. Shu, J. Messier, J. C. Wang, L. J. Burgt, K. Kountouriotis, Y. Xin, E. Holt, K. Schanze, R. Clark, T. Siegrist and B. W. Ma, One-dimensional organic lead halide perovskites with efficient bluish white-light emission, *Nat. Commun.*, 2017, **8**, 14051.

2 H. Yin, Q. K. Kong, R. L. Zhang, D. Y. Zheng, B. Yang and K. L. Han, Lead-free rare-earth double perovskite $Cs_2AgIn_{1-y-x}Bi_xLa_yCl_6$ nanocrystals with highly efficient warm-white emission, *Sci. China Mater.*, 2021, **64**, 2667–2674.

3 Y. Liu, F. D. Stasio, C. H. Bi, J. B. Zhang, Z. G. Xia, Z. F. Shi and L. Manna, Near-Infrared Light Emitting Metal Halides: Materials, Mechanisms, and Applications, *Adv. Mater.*, 2024, 2312482.

4 R. X. Wu, P. G. Han, D. Y. Zheng, J. F. Zhang, S. Q. Yang, Y. Zhao, X. Y. Miao and K. L. Han, All-Inorganic Rare-Earth-Based Double Perovskite Nanocrystals with Near-Infrared Emission, *Laser Photonics Rev.*, 2021, **15**, 2100218.

5 G. D. Zhang, P. P. Dang, H. Z. Lian, K. Li, L. Tian, W. Yang, Z. Y. Cheng and J. Lin, Assembling Two Self-Trapped Exciton Emissions in 0D Metal Halides with Near-Unity Quantum Yield and Zero Thermal-Quenching Photoluminescence, *Laser Photonics Rev.*, 2023, **18**, 2300599.

6 Y. Y. Jing, Y. Liu, J. Zhao and Z. G. Xia, Sb^{3+} Doping-Induced Triplet Self-Trapped Excitons Emission in Lead-Free Cs_2SnCl_6 Nanocrystals, *J. Phys. Chem. Lett.*, 2019, **10**, 7439–7444.

7 P. G. Han, C. Luo, S. Q. Yang, Y. Yang, W. Q. Deng and K. L. Han, All-Inorganic Lead-Free 0D Perovskites by a Doping Strategy to Achieve a PLQY Boost from <2% to 90%, *Angew. Chem., Int. Ed.*, 2020, **59**, 12709–12713.

8 X. Chen, Y. X. Pan, Y. H. Ding, H. Z. Lian, J. Lin and L. Y. Li, Enhanced Efficiency, Broadened Excitation, and Tailored Er^{3+} Luminescence Triggered by Te^{4+} Codoping in $Cs_2NaYbCl_6$ Crystals for Multifunctional Applications, *Inorg. Chem.*, 2024, **63**, 3525–3534.

9 Z. X. Zeng, G. D. Zhang, Y. S. Wang, M. Zhang, Z. Y. Cheng, H. Z. Lian and J. Lin, Mn^{2+}/Er^{3+}-Codoped $Cs_2AgInCl_6$ Double Perovskites with Dual Emission and Photochromism Properties for Anti-Counterfeiting Application, *Laser Photonics Rev.*, 2024, 2300983.

10 R. R. Sun, M. C. Jia, X. Chen, F. Zhang, Z. Z. Ma, Y. Liu, J. B. Zhang, L. Y. Lian, Y. B. Han, M. Y. Li, D. W. Yang, X. J. Li, Y. Zhang, C. X. Shan and Z. F. Shi, Constructing Efficient and Thermostable Red-NIR Emitter via Cross Relaxation and Crystal-Field Engineering of Holmium-Based Perovskite-Type Half Metal, *Laser Photonics Rev.*, 2023, 2301028.

11 F. Y. Zhao, Z. Song, J. Zhao and Q. L. Liu, Double perovskite $Cs_2AgInCl_6:Cr^{3+}$: broadband and near-infrared luminescent materials, *Inorg. Chem. Front.*, 2019, **6**, 3621–3628.

12 S. L. Jin, H. Yuan, T. Pang, M. J. Zhang, Y. W. He, B. Zhuang, T. M. Wu, Y. H. Zheng and D. Q. Chen, Boosting STE and Nd^{3+} NIR Luminescence in $Cs_2AgInCl_6$ Double Perovskite via Na^+/Bi^{3+}-Induced Local Structure Engineering, *Adv. Funct. Mater.*, 2023, **33**, 2304577.

13 K. Li and R. V. Deun, Novel Intense Emission-Tunable $Li_{1.5}La_{1.5}WO_6:Mn^{4+},Nd^{3+},Yb^{3+}$ Material with Good Luminescence Thermal Stability for Potential Applications in c-Si Solar Cells and Plant-Cultivation Far-Red-NIR LEDs, *ACS Sustainable Chem. Eng.*, 2019, **7**, 16284–16294.

14 K. Li and R. V. Deun, Effectively realizing broadband spectral conversion of UV/visible to near-infrared emission in $(Na,K)Mg(La,Gd)TeO_6:Mn^{4+},Nd^{3+},Yb^{3+}$ materials for c-Si solar cells via efficient energy transfer, *J. Mater. Chem. C*, 2018, **6**, 7302–7310.

15 B. M. Liu, X. X. Guo, L. Y. Cao, L. Huang, R. Zou, Z. Zhou and J. Wang, A High-efficiency blue-LED-excitable NIR-II-emitting $MgO:Cr^{3+},Ni^{2+}$ phosphor for future broadband light source toward multifunctional NIR spectroscopy applications, *Chem. Eng. J.*, 2023, **452**, 139313.

16 H. Arfin, A. S. Kshirsagar, J. Kaur, B. Mondal, Z. G. Xia, S. Chakraborty and A. Nag, ns^2 Electron (Bi^{3+} and Sb^{3+}) Doping in Lead-Free Metal Halide Perovskite Derivatives, *Chem. Mater.*, 2020, **32**, 10255–10267.

17 Z. C. Zeng, B. L. Huang, X. Wang, L. Lu, Q. Y. Lu, M. Z. Sun, T. Wu, T. F. Ma, J. Xu, Y. S. Xu, S. A. Wang, Y. P. Du and C. H. Yan, Multimodal Luminescent $Yb^{3+}/Er^{3+}/Bi^{3+}$-Doped Perovskite Single Crystals for X-ray Detection and Anti-Counterfeiting, *Adv. Mater.*, 2020, **32**, 2004506.

18 H. Arfin, J. Kaur, T. Sheikh, S. Chakraborty and A. Nag, $Bi^{3+}-Er^{3+}$ and $Bi^{3+}-Yb^{3+}$ Codoped $Cs_2AgInCl_6$ Double Perovskite Near-Infrared Emitters, *Angew. Chem., Int. Ed.*, 2020, **59**, 11307–11311.

19 Z. J. Shi, J. Guo, Y. H. Chen, Q. Li, Y. F. Pan, H. J. Zhang, Y. D. Xia and W. Huang, Lead-Free Organic–Inorganic Hybrid Perovskites for Photovoltaic Applications: Recent Advances and Perspectives, *Adv. Mater.*, 2017, **29**, 1605005.

20 M. B. Gray, S. Hariyani, T. A. Strom, J. D. Majher, J. Brgoch and P. M. Woodward, High-efficiency blue photoluminescence in the $Cs_2NaInCl_6:Sb^{3+}$ double perovskite phosphor, *J. Mater. Chem. C*, 2020, **8**, 6797–6803.

21 A. Noculak, V. Morad, K. M. McCall, S. Yakunin, Y. Shynkarenko, M. Wörle and M. V. Kovalenko, Bright Blue and Green Luminescence of Sb(III) in Double Perovskite Cs_2MInCl_6 (M = Na, K) Matrices, *Chem. Mater.*, 2020, **32**, 5118–5124.

22 L. Y. Cao, X. F. Jia, W. J. Gan, C. G. Ma, J. Y. Zhang, B. B. Lou and J. Wang, Strong Self-Trapped Exciton Emission and Highly Efficient Near-Infrared luminescence in $Sb^{3+}-Yb^{3+}$ Co-doped $Cs_2AgInCl_6$ Double Perovskite, *Adv. Funct. Mater.*, 2023, **33**, 2212135.

This journal is © the Partner Organisations 2024

Inorg. Chem. Front., 2024, **11**, 6146–6155 | **6153**

23 G. H. Wei, P. L. Li, R. Li, Y. Wang, S. X. He, J. L. Li, Y. W. Shi, H. Suo, Y. B. Yang and Z. J. Wang, How to Achieve Excellent Luminescence Properties of Cr Ion-Doped Near-Infrared Phosphors, *Adv. Opt. Mater.*, 2023, **11**, 2301794.

24 F. Q. He, E. H. Song, C. Zhang, H. Chang, G. P. Dong, Z. G. Xia, C. W. Wang and Q. Y. Zhang, $Cr^{3+} \leftrightarrow Fe^{3+}$ Energy Transfer Offset Enabling Anti-Thermal Quenching Near-Infrared Emission for Coded Wireless-Communication Applications, *Laser Photonics Rev.*, 2023, **18**, 2300668.

25 J. M. Xiang, X. Zhou, X. Q. Zhao, Z. Y. Wu, C. H. Chen, X. J. Zhou and C. F. Guo, Ab Initio Site-Selective Occupancy and Luminescence Enhancement in Broadband NIR Emitting Phosphor $Mg_7Ga_2GeO_{12}:Cr^{3+}$, *Laser Photonics Rev.*, 2023, **17**, 2200965.

26 Y. F. Pei, D. T. Tu, C. L. Li, S. Y. Han, Z. Xie, F. Wen, L. P. Wang and X. Y. Chen, Boosting Near-Infrared Luminescence of Lanthanide in $Cs_2AgBiCl_6$ Double Perovskites via Breakdown of the Local Site Symmetry, *Angew. Chem., Int. Ed.*, 2022, **61**, e202205276.

27 D. W. Chen, X. G. Zhang, J. W. Wei, L. Y. Zhou, P. C. Chen, Q. Pang and J. Z. Zhang, Simultaneous enhancement of near infrared luminescence and stability of $Cs_2AgInCl_6:Cr^{3+}$ double perovskite single crystals enabled by a Yb^{3+} dopant, *Inorg. Chem. Front.*, 2022, **9**, 4695–4704.

28 S. Saikia, A. Joshi, H. Arfin, S. Badola, S. Saha and A. Nag, Sb^{3+}-Er^{3+}-Codoped $Cs_2NaInCl_6$ for Emitting Blue and Short-Wave Infrared Radiation, *Angew. Chem., Int. Ed.*, 2022, **61**, e202201628.

29 J. Y. Sun, W. Zheng, P. Huang, M. R. Zhang, W. Zhang, Z. H. Deng, S. H. Yu, M. Y. Jin and X. Y. Chen, Efficient Near-Infrared Luminescence in Lanthanide-Doped Vacancy-Ordered Double Perovskite Cs_2ZrCl_6 Phosphors via Te^{4+} Sensitization, *Angew. Chem., Int. Ed.*, 2022, **61**, e202201993.

30 R. Q. Shi, S. H. Miao, X. L. Lv, D. X. Chen, Y. Zhang and Y. J. Liang, High-Efficiency Short-Wave Infrared Emitter Enabled by Cr^{3+}–Yb^{3+} Co-Doped Phosphor, *Adv. Opt. Mater.*, 2024, 2303221.

31 Y. N. Wang, M. M. Shang, S. Huang, Y. X. Sun, Y. Y. Zhu, X. L. Xing, P. P. Dang and J. Lin, Continuous Ultra-Broadband Near-Infrared Sc_2O_3-Based Nanophosphor Realized by Spectral Bridge of Cr^{3+}-Yb^{3+}-Cr^{4+} for Multiple Optical Applications, *Adv. Opt. Mater.*, 2023, **11**, 2300517.

32 S. Y. Han, D. T. Tu, Z. Xie, Y. Q. Zhang, J. Y. Li, Y. F. Pei, J. Xu, Z. L. Gong and X. Y. Chen, Unveiling Local Electronic Structure of Lanthanide-Doped $Cs_2NaInCl_6$ Double Perovskites for Realizing Efficient Near-Infrared Luminescence, *Adv. Sci.*, 2022, **9**, 2203735.

33 G. D. Zhang, Y. Wei, P. P. Dang, H. Xiao, D. J. Liu, X. K. Li, Z. Y. Cheng and J. Lin, Facile solution synthesis of Bi^{3+}/Yb^{3+} ions co-doped $Cs_2Na_{0.6}Ag_{0.4}InCl_6$ double perovskites with near-infrared emission, *Dalton Trans.*, 2020, **49**, 15231–15237.

34 S. Yang, S. F. Gong, Z. L. Zhou, L. F. Wu, M. M. Zhang, L. L. Jiang and W. Z. Wu, Bi and Yb Codoped $Cs_2Ag_{0.6}Na_{0.4}InCl_6$ Microcrystals: Visible to Near-Infrared Fluorescence for Thermometry, *J. Phys. Chem. C*, 2021, **125**, 10431–10440.

35 B. Zhou, Z. X. Liu, S. F. Fang, H. Z. Zhong, B. B. Tian, Y. Wang, H. N. Li, H. L. Hu and Y. M. Shi, Efficient White Photoluminescence from Self-Trapped Excitons in Sb^{3+}/Bi^{3+}-Codoped $Cs_2NaInCl_6$ Double Perovskites with Tunable Dual-Emission, *ACS Energy Lett.*, 2021, **6**, 3343–3351.

36 B. Zhou, A. X. Du, D. Ding, Z. X. Liu, Y. Wang, H. Z. Zhong, H. N. Li, H. L. Hu and Y. M. Shi, Achieving Tunable Cold/Warm White-Light Emission in a Single Perovskite Material with Near-Unity Photoluminescence Quantum Yield, *Nano-Micro Lett.*, 2023, **15**, 207.

37 F. Zhang, X. Chen, X. F. Qi, W. Q. Liang, M. Wang, Z. Z. Ma, X. Z. Ji, D. W. Yang, M. C. Jia, D. Wu, X. J. Li, Y. Zhang, Z. F. Shi and C. X. Shan, Regulating the Singlet and Triplet Emission of Sb^{3+} Ions to Achieve Single-Component White-Light Emitter with Record High Color-Rendering Index and Stability, *Nano Lett.*, 2022, **22**, 5046–5054.

38 W. G. Huang, H. Peng, Q. L. Wei, J. J. Xia, X. F. He, B. Ke, Y. Tian and B. S. Zou, Tunable Efficient White Emission in Holmium Doped Double Perovskites Cs_2KInCl_6 via Antimony Sensitization, *Adv. Opt. Mater.*, 2023, **11**, 2203103.

39 W. J. Gan, L. Y. Cao, S. M. Gu, H. W. Lian, Z. G. Xia and J. Wang, Broad-Band Sensitization in Cr^{3+}–Er^{3+} Co-Doped $Cs_2AgInCl_6$ Double Perovskites with 1.5 μm Near-Infrared Emission, *Chem. Mater.*, 2023, **35**, 5291–5299.

40 H. W. Li, K. Han, Z. Y. Li, H. X. Yue, X. Y. Fu, X. Y. Wang, Z. G. Xia, S. Y. Song, J. Feng and H. J. Zhang, Multiple Energy Transfer Channels in Rare Earth Doped Multi-Exciton Emissive Perovskites, *Adv. Sci.*, 2023, **11**, 2307354.

41 R. S. Zeng, L. L. Zhang, Y. Xue, B. Ke, Z. Zhao, D. Huang, Q. L. Wei, W. C. Zhou and B. S. Zou, Highly Efficient Blue Emission from Self-Trapped Excitons in Stable Sb^{3+}-Doped $Cs_2NaInCl_6$ Double Perovskites, *J. Phys. Chem. Lett.*, 2020, **11**, 2053–2061.

42 P. Huang, W. Zheng, D. T. Tu, X. Y. Shang, M. R. Zhang, R. F. Li, J. Xu, Y. Liu and X. Y. Chen, Unraveling the Electronic Structures of Neodymium in $LiLuF_4$ Nanocrystals for Ratiometric Temperature Sensing, *Adv. Sci.*, 2019, **6**, 1802282.

43 Y. Li, J. Wang, W. L. Zhou, G. G. Zhang, Y. Chen and Q. Su, Ultraviolet–Visible–Near-Infrared Luminescence Properties and Energy Transfer Mechanism of a Novel 5d Broadband Sensitized $Sr_3SiO_5:Ce^{3+},Yb^{3+}$ Suitable for Solar Spectral Converter, *Appl. Phys. Express*, 2013, **6**, 082301.

44 M. N. Tran, I. J. Cleveland, G. A. Pustorino and E. S. Aydil, Efficient near-infrared emission from lead-free ytterbium-doped cesium bismuth halide perovskites, *J. Mater. Chem. A*, 2021, **9**, 13026–13035.

45 Y. H. Wang, S. C. Bai, J. Sun, H. Liang, C. Li, T. Y. Tan, G. Yang and J. W. Wang, Highly efficient visible and near-infrared luminescence of Sb^{3+}, Tm^{3+} co-doped Cs_2NaYCl_6

6154 | *Inorg. Chem. Front.*, 2024, **11**, 6146–6155

This journal is © the Partner Organisations 2024

lead-free double perovskite and light emitting diodes, *J. Alloys Compd.*, 2023, **947**, 169602.

46 Z. C. Liu, Y. X. Pan, C. D. Peng, Y. H. Ding, H. Z. Lian, J. Lin and L. Y. Li, Enhancing Luminescence in Hue-Tunable White-Light Emitting K_4CdCl_6:Sb^{3+},Mn^{2+} All-Inorganic Halide Perovskites: Insights from Defect Engineering and Energy Transfer, *ACS Appl. Mater. Interfaces*, 2023, **15**, 51462–51473.

47 D. C. Yu, F. T. Rabouw, W. Q. Boon, T. Kieboom, S. Ye, Q. Y. Zhang and A. Meijerink, Insights into the energy transfer mechanism in Ce^{3+}-Yb^{3+} codoped YAG phosphors, *Phys. Rev. B: Condens. Matter Mater. Phys.*, 2014, **90**, 165126.

48 A. D. Sontakke, J. Ueda, Y. Katayama, P. Dorenbos and S. Tanabe, Experimental insights on the electron transfer and energy transfer processes between Ce^{3+}-Yb^{3+} and Ce^{3+}-Tb^{3+} in borate glass, *Appl. Phys. Lett.*, 2015, **106**, 131906.

49 Z. Barandiarán, A. Meijerinkc and L. Seijo, Configuration coordinate energy level diagrams of intervalence and metal-to-metal charge transfer states of dopant pairs in solids, *Phys. Chem. Chem. Phys.*, 2015, **17**, 19874–19884.

50 B. Chen, Y. Guo, Y. Wang, Z. Liu, Q. Wei, S. X. Wang, A. L. Rogach, G. C. Xing, P. Shi and F. Wang, Multiexcitonic Emission in Zero-Dimensional Cs_2ZrCl_6:Sb^{3+} Perovskite Crystals, *J. Am. Chem. Soc.*, 2021, **143**, 17599–17606.

51 C. Wang, Y. Liu, X. Feng, C. Y. Zhou, Y. L. Liu, X. Yu and G. J. Zhao, Phase Regulation Strategy of Perovskite Nanocrystals from 1D Orthomorphic NH_4PbI_3 to 3D Cubic $(NH_4)_{0.5}Cs_{0.5}Pb(I_{0.5}Br_{0.5})_3$ Phase Enhances Photoluminescence, *Angew. Chem., Int. Ed.*, 2019, **58**, 11642–11646.

52 C. Wang, N. J. Zhao, H. Y. Zhang, X. F. Zhang, X. H. Lin, H. Liu, F. Dang, W. Zhang, J. Sun, P. Chen, H. L. Chen, P. G. Han and P. Li, Ultrawide UV to NIR Emission in Double Perovskite Nanocrystals via the Self-Trapping State Engineering Strategy, *ACS Sustainable Chem. Eng.*, 2023, **11**, 14659–14666.

53 Y. R. Guo, H. W. Guan, P. Li, C. Wang, Y. Wang, J. R. Zhang and G. J. Zhao, Non-adiabatic conformation distortion charge transfer enables dual emission of thermally activated delayed fluorescence and room temperature phosphorescence, *Spectrochim. Acta, Part A*, 2024, **311**, 124032.